Modifying the crystallization of amorphous magnesium-calcium phosphate nanoparticles with proteins from Moringa oleifera seeds

Contents lists available at ScienceDirect

Journal of Colloid and Interface Science

journal homepage: http://ees.elsevier.com

Regular Article

Modifying the crystallization of amorphous magnesium-calcium phosphate nanoparticles with proteins from *Moringa oleifera* seeds

Rita Gelli [a,1], Monica Tonelli [a,1], Francesca Ridi [a], Massimo Bonini [a], Habauka M. Kwaambwa [b], Adrian R. Rennie [c,*], Piero Baglioni [a,*]

[a] Department of Chemistry "Ugo Schiff" and CSGI, University of Florence, via della Lastruccia 3, 50019 Sesto Fiorentino, Florence, Italy
[b] Faculty of Health and Applied Sciences, Namibia University of Science and Technology, Private Bag 13388, 13 Jackson Kaujeua Street, Windhoek, Namibia
[c] Centre for Neutron Scattering, Uppsala University, Box 516, 751 20 Uppsala, Sweden

ARTICLE INFO

Article history:
Received 17 November 2020
Received in revised form 3 January 2021
Accepted 4 January 2021
Available online xxx

Keywords
Amorphous Mg-Ca phosphates
Moringa oleifera
AMCP/MO hybrid nanoparticle/microparticle
Amorphous stabilization
Crystallization

ABSTRACT

Hypothesis: Endogenous Amorphous Magnesium-Calcium Phosphates (AMCPs) form in the human body and, besides their biomedical implications, the development of effective stabilization strategies is an open challenge. An interesting approach consists of stabilizing amorphous phosphates with macromolecules that have beneficial effects from a nutritional/medical point of view, for a potential application of the hybrid particles in nutraceutics or drug delivery.

Experimental: We investigated the effect of proteins extracted from *Moringa oleifera* seeds (MO) on the features of synthetic analogs of AMCPs and on their crystallization pathway. The stability of the amorphous phase was studied using infrared spectroscopy and X-ray diffraction. To unravel the effect of the protein on the nano-scale structure of the inorganic particles, we also studied how MO affects the features of the amorphous phase using thermal analysis, small angle X-ray scattering and confocal Raman microscopy.

Findings: We observed that MO markedly delays the transition from amorphous to crystalline phosphate in a concentration-dependent fashion. Interestingly, MO not only enhances the lifetime of the amorphous phase, but also influences the type and amount of crystalline material formed. The results are relevant from both a fundamental and an applied perspective, paving the way for the use of these hybrids in the field of nutraceutics and drug delivery.

1. Introduction

Among the variety of Amorphous Calcium Phosphate (ACP)-based structures present in our body [1], the recently-discovered Amorphous Magnesium-substituted Calcium Phosphate (AMCP) particles which form in mammalian small intestines, represent a particularly interesting case study [2]. These nano- and micro-minerals are believed to be involved in immune-surveillance mechanisms, as they were observed to bind antigens and peptidoglycans and to transport them to the immune cells of the intestinal tissue [2]. Besides the biomedical implications of this process [3,4], the full understanding of the formation and the features of these particles opens up a series of intriguing physico-chemical aspects. Endogenous AMCPs possess a porous and amorphous structure, have a size of 75–150 nm and are composed of Ca, Mg, Na, O and P [2,5]. The amorphous nature is intriguing as AMCPs, and more in general ACPs, are well-known to be highly unstable in aqueous media, given their tendency to evolve into a more thermodynamically stable form of crystalline calcium or magnesium phosphate [6]. The fact that such unstable structures repeatedly form in the human gut highlights the importance of amorphous phosphates to the functioning of the body organs and emphasizes the importance of *seeking new strategies to prolong the lifetime of AMPCs amorphous phase.* Ions, such as Mg^{2+} [7–15], Ga^{3+} [16], Cd^{2+} [17], Sr^{2+} [8,18], Zn^{2+} [19], $P_2O_7^{4-}$ [18,20,21], CO_3^{2-} [22] and citrate [23], have been shown to delay to a different extent the transition from amorphous to crystalline calcium phosphates. The effects of some biologically-relevant molecules and macromolecules were also investigated previously, and the stabilizing action of adenosine triphosphate [24–27], bile salts [28] and proteoglycans [29,30] is described in the literature. Some synthetic polymers also display the ability to slow down the conversion of ACP to crystalline calcium phosphate and the relevant examples include PEG (poly(ethylene glycol)) [31,32], PAA (poly(acrylic acid)) [33,34], as well as a range of other synthetic anionic and cationic polyelectrolytes, [35] and poly(amino acids) [20,36]. In general, ions and molecules

* Corresponding authors.
E-mail addresses: adrian.rennie@physics.uu.se (A.R. Rennie); baglioni@csgi.unifi.it (P. Baglioni)
[1] These authors equally contributed to this work.

https://doi.org/10.1016/j.jcis.2021.01.008
0021-9797/

that are present during the synthesis of ACP can be incorporated within the structure, possibly leading to a modification in the atomic arrangement of the clusters composing the amorphous phase. Although ACP can be stabilized to some extent with the cited additives, its intrinsic metastable nature will eventually lead to the transformation into a crystalline phosphate [37]. *Therefore, the quest for effective strategies to enhance the stability of amorphous phosphates is an open challenge*. A captivating approach consists of stabilizing ACP/AMCP with molecules or macromolecules which have beneficial effects from a nutritional or medical point of view, for a potential application in nutraceutics or drug delivery. This strategy has a two-fold relevance as the molecule, while acting as stabilizing agent for the amorphous phase, could eventually be released from the hybrid to fulfil a specific function. Nanocarriers are in fact frequently used to load food products in order to improve their bioavailability and protect valuable nutraceuticals during food processing or digestion [38]. The possibility of using AMCP for the loading of active components is straightforward if the biological function in the mammalian ileum is recalled, *i.e.* the loading of macromolecules (dietary antigens and peptidoglycans) and the release of the organic cargo to antigen-presenting cells [2].

Among the bio-relevant macromolecules whose effect as stabilizers for AMCP has never been investigated so far, proteins extracted from *Moringa oleifera* (MO) represent an interesting case study. MO is a tree native to tropical and subtropical regions of south Asia that is now also widespread in Africa and South America. Sometimes referred to as "the miracle tree", this plant can grow quickly even on soils having relatively low humidity, and it is known to be non-toxic to humans and animals. It has an impressive range of medicinal uses, including the control of disorders of circulatory system, the improvement of the function of the digestive tract, to the treatment of arthritis, kidney stones, inflammations and anemia. Different parts of this plant (roots, seeds, leaves, flowers) contain a profile of important minerals and are a good source of proteins, vitamins, β-carotene, amino-acids and various phenols [39], making its use as dietary supplement well established. Seeds are reported to have antimicrobial activity [39] and are widely employed for the treatment of water and wastewater, due to the action of the cationic proteins which are responsible for the coagulation and flocculation mechanisms [40] (the isoelectric point is around pH = 10 [41]). In the framework of inorganic phosphate precipitation, given their positively-charged nature [42,43], these proteins are expected to interact with ions present in AMCP-forming solution, thus having an impact on its formation and crystallization pathways. The effect of MO on calcium phosphate precipitation is scarcely documented in the literature. Some examples show the possibility of using MO flower extracts to prepare hydroxyapatite-based nanorods [44] and nanoplates [45]. On the other hand, the potential of calcium phosphates for the loading and release of proteins has been reported for bovine serum albumin [46–48] and bone morphogenetic protein [49]. In principle, the amorphous and porous nature of AMCP should improve the loading capability of the inorganic structure.

The aim of this study was to assess the effect of proteins extracted from *Moringa oleifera* seeds on the features of endogenous-like AMCPs and on their crystallization pathway. Amorphous nanoparticles were prepared with an aqueous-based synthesis in the presence of different concentrations of protein, and their evolution with time was investigated focusing on the effect of MO on both the crystallization pathway and on the features of the amorphous phase.

2. Materials and methods

2.1. Samples' preparation

2.1.1. Materials

Sodium phosphate monobasic ($NaH_2PO_4{\cdot}H_2O$, ≥99%) and sodium phosphate dibasic ($Na_2HPO_4{\cdot}12H_2O$, ≥99%) were purchased from Carlo Erba Reagents (Milan, Italy). Sodium chloride (NaCl, ≥99%), calcium chloride ($CaCl_2$, ≥93%) and magnesium chloride ($MgCl_2{\cdot}6H_2O$, ≥99%) were obtained from Sigma-Aldrich (Milan, Italy). MilliQ water was used during all the experiments.

Moringa oleifera seeds were obtained from Mahalapye, Botswana. MO protein was extracted and purified by the method of Ndabigengesere and Narasiah, as previously reported in the literature [41,50,51].

2.1.2. Synthesis of AMCPs

AMCPs were prepared by mixing equal volumes (20 mL) of two solutions, namely solution A (which contains NaH_2PO_4 and Na_2HPO_4) and solution B (NaCl, $CaCl_2$ and $MgCl_2$). The concentrations and amounts of salts in these solutions are given in Table 1. Solutions A and B were prepared by dissolving salts in water and the flasks were separately heated at 37 °C in a water bath. After mixing the solutions, the temperature and the pH of the dispersion was monitored through the entire synthesis and, when necessary, the pH was maintained at 7.30 ± 0.02 by dropwise addition of NaOH 1 M or HCl 1 M. Aliquots of 5 mL were withdrawn after 15 min, 30 min, 60 min, 90 min, 2 h, 6 h, 24 h and 48 h. The collected solutions were centrifuged at 6000 rpm for 3 min and the supernatant was discarded. The particles were washed with 5 mL of absolute ethanol and centrifuged (6000 rpm, 3 min) three times, dried under nitrogen flux and kept for 30 min under vacuum. Specimens were stored at −18 °C to prevent a spontaneous crystallization.

The three syntheses conducted using the same procedure were pristine nanoparticles (AMCP), particles prepared in the presence of 1 mg/mL of Moringa protein (AMCP_1MO) and particles prepared in the presence of 10 mg/mL of protein (AMCP_10MO). When present, MO (40 mg and 400 mg, respectively) was dispersed in 2 mL of water and simultaneously mixed with 19 mL of solution A and 19 mL of B.

2.2. Characterization techniques

2.2.1. Fourier transform-infrared spectroscopy (FT-IR)

FT-IR spectra were collected using a Bio-Rad FTS-40 spectrophotometer (Hercules, CA, USA). The samples were analyzed in KBr pellets prepared by mixing 1.00 ± 0.05 mg of sample with 100.0 ± 0.1 mg of KBr (Sigma-Aldrich, FT-IR grade). The spectra were acquired in the range 4000–400 cm^{-1} using a resolution of 2 cm^{-1}, 64 scans and scan delay of 600 s.

2.2.2. X-ray diffraction (XRD)

XRD data were collected with a D8 Advance with DAVINCI design (Bruker, Milan, Italy), using as X-rays source the Cu Kα radiation (wavelength k = 1.542 Å), at 40 kV and 40 mA, a 2θ range of 10–60°, a step size of 0.03°, and a time/step of 0.3 s. A Si zero-background sample holder was used, while the assignment of peaks was based on the Powder Diffraction Files (PDF) of the ICDD database (International Centre for Diffraction Data).

For the quantitative XRD analyses (AMCP_48h, AMCP_1MO_48h and AMCP_10MO_48h), the diffractograms were collected using glass capillaries (0.3 mm diameter), at 40 kV and 40 mA, a 2θ range of 5–80°, a

Table 1
Composition of the 50 mL solutions used for the synthesis of AMCPs.

	Salts	Concentration [mM]	Amount [g]
A	$NaH_2PO_4{\cdot}H_2O$	50	0.345
	$Na_2HPO_4{\cdot}12H_2O$	150	2.686
B	NaCl	135	0.395
	$CaCl_2$	40	0.222
	$MgCl_2{\cdot}6H_2O$	100	1.017

step size of 0.01°, and a time/step of 4 s. The relative amounts of the formed phases were estimated by means of the Rietveld method using the software Topas (Bruker). The CIF (Crystallographic Information File) data used for the analysis were obtained from the American Mineralogist Crystal Structure Database (0009313 for newberyite and 0001049 for baricite) and Crystallography Open Database (9001026 for bobierrite). The error associated with the fitting is 1%, with $R_{wp} < 5$.

2.2.3. Field emission-scanning electron microscopy (FE-SEM)

FE-SEM analysis was conducted using a Zeiss SIGMA FE-SEM (Carl Zeiss Microscopy GmbH, Jena, Germany). The powders (specimens obtained after 15 min, 30 min, 24 h and 48 h) were placed over aluminum stubs by means of conductive tape. The micrographs were acquired with an accelerating voltage of 2 kV, sample-detector distance ~4 mm and using the In-Lens detector.

2.2.4. Simultaneous differential scanning calorimetry/thermogravimetry (SDT)

SDT analyses were performed using SDT Q600 from TA Instruments (New Castle, DE, USA). Each sample (AMCP_15min, AMCP_1MO_15min and AMCP_10MO_15min) was placed in an alumina pan and measurements were conducted in N_2 atmosphere (flow rate 100 mL/min) from room temperature to 1000 °C, at 10 °C/min.

SDT was also used to obtain the activation energies (E_a) of the heat-induced crystallization of the amorphous phase. Following instrumental calibration at different heating rates, samples were analyzed at 5, 10, 20 and 50 °C/min, and the shift of the crystallization peak was used to estimate E_a using the Kissinger method [52], which correlates the heating rate (β, K/min) with the peak temperature (T_p). E_a can thus be calculated according to Eq. (1)

$$\ln\left(\frac{\beta}{T_p^2}\right) = -\frac{E_a}{R\cdot T_p} + \ln\left(\frac{A\cdot R}{E_a}\right) \quad (1)$$

where R is the universal gas constant and A the pre-exponential factor. The method only holds for first order reaction kinetics and for $\beta > 0$ (heating experiments) [53]. The experimental error associated to T_p is ±2 K.

The reaction order was further assessed by means of the Borchardt–Daniels method [54], by selecting 10 points within the crystallization peak of the 10 °C/min curve, between the onset and the maximum. At each temperature, the intensity of the heat flow (dH) at different times and the corresponding ΔH, the heat generated at the temperature T in the corresponding time interval (ΔH = dH/dt) were calculated. According to the method, the rate constants *k* at different temperatures and for different reaction orders, *n*, can be calculated using the following expressions

$$k_0 = \frac{\Delta H}{S_0} \quad \text{for } n = 0 \quad (2)$$

$$k_{1/2} = \frac{\Delta H}{\left\{2S_0\left[1-\left(S_T-S_0\right)\right]\right\}^{1/2}} \quad \text{for } n = 1/2 \quad (3)$$

$$k_{2/3} = \frac{\Delta H}{\left\{3S_0\left[1-\left(S_T-S_0\right)\right]\right\}^{2/3}} \quad \text{for } n = 2/3 \quad (4)$$

$$k_1 = \frac{\Delta H}{S_T - S_0} \quad \text{for } n = 1 \quad (5)$$

where S_0 is the total integrated peak intensity and S_T is the integrated peak intensity from the beginning of the peak to the temperature T. From a plot of ln k vs 1/T for every *n*, the reaction order that describes the system is chosen on the basis of the best correlation coefficient obtained.

2.2.5. Small angle X-ray scattering (SAXS)

SAXS experiments were carried out with a S3-MICRO instrument (HECUS GmbH, Graz, Austria) equipped with a position-sensitive detector (OED 50 M) containing 1024 channels of width 54 μm. Cu Kα radiation (λ = 1.542 Å) was provided by a GeniX X-ray source (Xenocs, Grenoble, France), operating at 12 W (30 kV and 0.4 mA). Powder samples were sealed in a cell between two Kapton windows, and each data set was collected for 2 h at 25 °C. The volume between the sample and the detector was kept under vacuum during the measurements to minimize scattering from air. The sample-detector distance (281 mm) was calibrated by measuring the scattering pattern of silver behenate. Scattering curves were obtained in the q-range between 0.008 and 0.5 $Å^{-1}$, where $q = (4\pi/\lambda)\cdot\sin(\theta/2)$ is the scattering vector and θ the scattering angle, and they were corrected for the empty cell (*i.e.*, Kapton) contribution by adjusting their relative transmissions (data are not in absolute scale).

Scattering curves were fitted with the SasView software (Version 4.2.2 [55]). Different models were tested to account for the presence of nanostructures in the accessible length scale: the shape-independent multi-level approach by Beaucage (also known as the Unified Fit approach) [56–58], the Teixeira Model for the scattering from a fractal structure formed from core shell spheres [59] and the Guinier-Fournet form factor for polydisperse spherical particles with a core–shell structure [60], including the Percus-Yevick inter-particle structure factor of hard spheres [61], and mixtures of them. The patterns of deviations (*i.e.*, the residual values at different scattering vector values) were used to evaluate the goodness of the fit. The scattering length densities (SLDs) of AMCP and MO, when needed in the model, were calculated according to their composition and densities. The SLD of the solvent (vacuum in our case) was taken as equal to zero. More details are given in the Supporting Information section.

2.2.6. Confocal Raman microscopy

Raman analysis and mapping were performed on a Renishaw inVia Qontor confocal MicroRaman system equipped with 532 nm laser (Nd:YAG solid state type, 50 mW, 1800 l/mm grating), front illuminated CCD camera (256 × 1024 pixels, −70 °C) and research-grade Leica DM 2700 microscope equipped with 100× objective (NA 0.85, WD 0.27 mm). Powder samples were placed between two glass slides. A Raman spectrum was acquired for AMCP_15min and pristine MO in the range 3100–300 cm^{-1}, while AMCP_1MO_15min and AMCP_10MO_15min were mapped with an accumulation time of 10 s using the two distinct signals of AMCPs and MO (located at 700–1100 cm^{-1} and 2800–3100 cm^{-1}, respectively). Maps were collected with a step size of 1 μm (slightly larger than the nominal objective resolution in these experimental conditions).

3. Results and discussion

3.1. Characterization of the amorphous-to-crystalline transition

The stability of AMCPs was investigated by FT-IR and XRD analyses to evaluate the effect of different amounts of MO on the crystallization process of the particles. The shape and the position of the IR peaks (see Fig. 1) reveal that the initially-formed precipitate in all samples is an amorphous phosphate displaying broad bands, which then converts to crystalline phases when sharp and distinctive signals appear [15,62]. The presence of amorphous particles at short times is confirmed by the broad and featureless bands associated with hydroxyl stretching (3700–2500 cm^{-1} region), water HOH-bending (1900–1300 cm^{-1}) and P—O stretching vibrations (1200–400 cm^{-1}) [63]. In the absence of MO (Fig. 1A), AMCPs crystallization occurs within 30 min, while in AMCP_1MO (Fig. 1B), the particles turn crystalline after about 2 h and in AMCP_10MO (Fig. 1C) the first signatures of crystallinity appear after

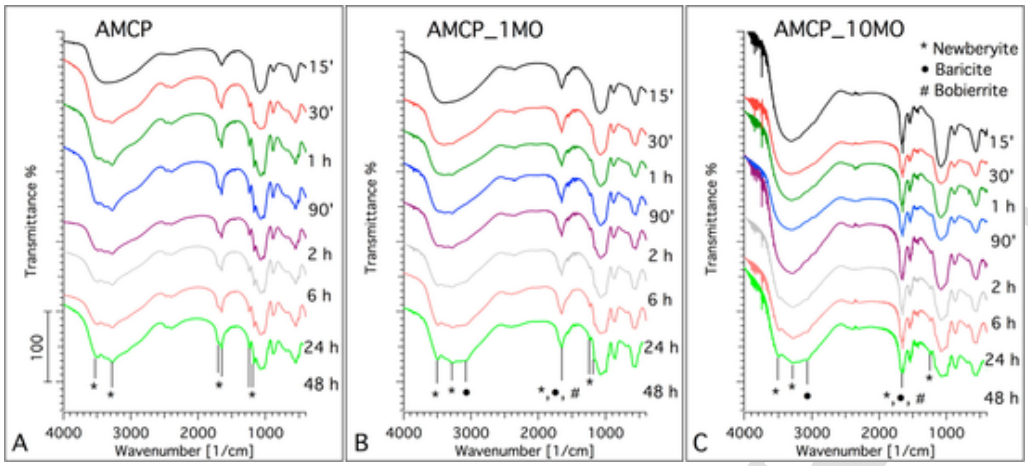

Fig. 1. FT-IR spectra of AMCP (A), AMCP_1MO (B) and AMCP_10MO (C). The time after which each aliquot was withdrawn from the solution is given on the right of each curve. Symbols indicate the most diagnostic signals for the three phases present in the samples. The spectra have been offset for the sake of clarity.

6 h. The spectra of the phases formed upon crystallization are compatible with the presence of newberyite ($MgHPO_4{\cdot}3H_2O$), bobierrite and baricite ($Mg_3(PO_4)_2{\cdot}8H_2O$) [64,65]. The latter phases share the same chemical composition; however, they are characterized by different space groups (monoclinic C2/m for baricite and monoclinic C2/c for bobierrite). Comparing the 48 h-spectra, some differences can be observed. In Fig. 1, some characteristic peaks of newberyite, baricite and bobierrite are labelled, and it can be observed that the relative ratio between the forming crystalline phases is different between the samples. This result shows that MO not only extends the lifetime of the amorphous phase in solution, but it also affects the relative ratio between the crystalline phases, favouring the formation of baricite and bobierrite over newberyite, as confirmed by XRD analysis discussed below. Moreover, in AMCP_10MO spectra an additional peak at ~1550 cm^{-1} was observed, which is consistent with the incorporation of MO in the samples [66], as confirmed by confocal Raman microscopy (Section 3.2).

Given that quantitative information on the crystallinity cannot be directly obtained by means of FT-IR, the crystallization process and the nature of the crystalline phases formed upon conversion of AMCPs were further investigated by means of XRD analysis (see Fig. 2). As previously reported in the literature [15], AMCPs display a broad peak centered at ~30°, and in all samples the product collected after 15 min is amorphous. When the amorphous structure converts to crystalline phases, sharp signals appear, confirming the presence of newberyite, baricite and bobierrite phases. The qualitative analysis of the XRD diffractograms confirms the conclusions drawn from infrared spectroscopy, *i.e.* the lifetime of the amorphous phase increases in presence of MO and the more protein was added, the more the conversion of the particles to crystalline phases retarded.

If the intensities of the diffraction peaks of the samples collected after 48 h are compared, it is evident that the relative intensities of the diagnostic peaks of the amorphous and crystalline phases are different. In the presence of MO (Fig. 2B and C), diffraction peaks for newberyite are less intense compared to those of baricite and bobierrite. At the same time, in AMCP sample (Fig. 2A) the crystalline phases predominate, while in AMCP_10MO (Fig. 2C) the broad signal at about 30°, characteristic of the amorphous phase, is still evident. In order to estimate the relative amounts of amorphous and crystalline phases on 48 h samples, a quantitative Rietveld analysis was performed and the results are reported in Table 2 (patterns and fitting analyses are shown in Fig. S1 in the Supporting Information). For the fitting, the amount of amorphous AMCPs was calculated between 21 and 31°, while for the crystalline phases CIF data were used (as reported in Section 2.2.2). Consistent with the qualitative observations of the diffraction peak intensities, the relative amount of crystalline phases decreases with the increase of protein concentration, and newberyite is markedly less abundant in the presence of MO. The results of the fitting thus confirm that MO has a twofold effect on AMCPs: it delays the amorphous-to-crystalline transition and modifies the crystallization pathway of the amorphous particles by favouring the crystallization of baricite and bobierrite over newberyite.

The effect of MO on the preferential crystallization of baricite and bobierrite could be related to electrostatic interactions. According to

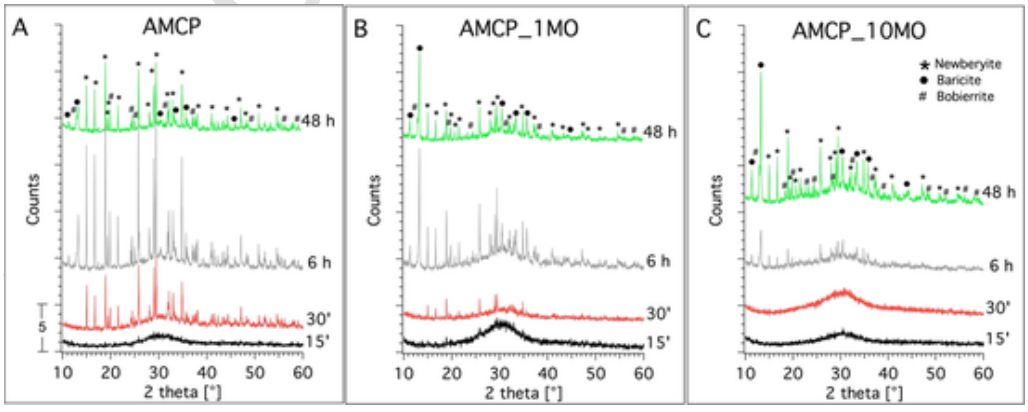

Fig. 2. XRD patterns of AMCP (A), AMCP_1MO (B) and AMCP_10MO (C). The time after which each aliquot was withdrawn from the solution is given on the right of each curve. The PDF used for peaks' assignment are n° 70-2345 for newberyite, n° 29-0705 for baricite and n° 33-0878 for bobierrite. The patterns have been offset for clarity of display.

Table 2
Relative amounts of amorphous and crystalline phases obtained by means of a Rietveld fitting on the recorded diffractograms. The error associated with the fitting is 1%.

	Relative amounts of phases (±1%)				
	Amorphous	Crystalline	Newberyite	Baricite	Bobierrite
AMCP_48h	12	88	60	16	12
AMCP_1MO_48h	15	85	31	31	23
AMCP_10MO_48h	17	83	29	32	22

the literature, the formation of ACP occurs in condition of high supersaturation, where calcium/magnesium cations and phosphate anions are sufficiently abundant to involve strong stochastic interactions, and the amorphous particles precipitate as a result of a kinetic phenomenon [67]. The conversion of these unstable particles to crystalline phases proceeds by a sequential process, which involves structural and compositional modifications of the amorphous precursors and crystalline intermediates [1]. It is important to point out that the pH was kept constant at 7.30 ± 0.02, therefore the different crystallization processes observed are related to MO presence in solution. At this pH, MO is positively charged [41] and it is expected to preferentially interact with negatively-charged species, such as phosphate. This could locally lead to a preferential formation of PO_4^{3-} over HPO_4^{2-} in the proximity of the amorphous cluster, which eventually lead to the precipitation of bobierrite and baricite ($Mg_3(PO_4)_2{\cdot}8H_2O$) over newberyite ($MgHPO_4{\cdot}3H_2O$).

The morphology of the amorphous and crystalline samples was studied with FE-SEM, and the micrographs at 15 min and 48 h are reported in Fig. 3 (see Fig. S2 for the micrographs at 30 min and 6 h). Amorphous samples show the characteristic spherical particles as reported in the literature for AMCPs [15], which then evolve to more ordered structures during crystallization. The size distribution of the single objects observed in the 15 min samples is reported in Fig. S3 and reveals an average diameter around 60 nm. At the length scales accessible by FE-SEM, the presence of MO does not affect the morphology, or the size of the amorphous particles precipitated after 15 min (Fig. 3 top), whereas it influences the morphology of the samples at longer times. In fact, comparing the morphology of samples collected after 30 min and 24 h (Fig. S2), the number of crystalline objects decreases with the increase of MO, consistent with FT-IR and XRD analyses, while flake-like objects replace part of the spherical AMCPs in the presence of the protein. After 48 h, crystals form upon conversion of AMCPs in all samples (Fig. 3 bottom).

3.2. Effect of MO on the features of the amorphous phases

Since MO markedly affects the lifetime of the amorphous phase and its crystallization pathway in solution, it was necessary to understand if this could be due to a direct effect of the protein on the features of the amorphous phase formed in the early stages of the reaction. The samples collected were analyzed after 15 min by means of SDT in order to investigate their thermal decomposition and thus quantify the amount of organic material incorporated in the amorphous particles. The thermogravimetric curves, displayed in green in Fig. 4, show that at 1000 °C AMCP has lost 24%, whereas AMCP_1MO and AMCP_10MO lost 27% and 35% of their initial weight, respectively. The higher weight loss of samples containing MO can be ascribed to the thermal degradation of the protein, which is therefore present in the samples at 3% in AMCP_1MO and 11% in AMCO_10MO (assuming its complete degradation at 1000 °C). The analysis of the derivative weight % signals (blue curves in Fig. 4) further highlights the degradation of the protein, which mainly occurs at 200–400 °C and 500–600 °C. In sample AMCP_10MO_15′, the weight losses centred at about 300 °C and 580 °C reflect the highest content of MO in the sample. These results are consistent with FT-IR analysis, showing that MO can be effectively incorporated within AMCP. It is worth noting that the amount of protein present in the particles does not correspond to the total amount used in the synthesis, *i.e.*, incorporated MO in AMCP_1MO is 21% wt of the initial MO amount, while in AMCP_10MO it is 18% wt, suggesting that only a fraction of the protein interacts with AMCP.

The analysis of the heat flow profiles (red curves in Fig. 4) gives insights on the heat-induced crystallization processes, connected to the features of the amorphous phase [68]. The samples display an exothermic peak at about 600 °C which is due to the conversion of AMCP towards a crystalline sodium calcium magnesium phosphate ($Ca_9MgNa(PO_4)_7$, PDF 45-0136), as we previously reported [15]. In the samples containing MO, this heat-induced crystallization does not oc-

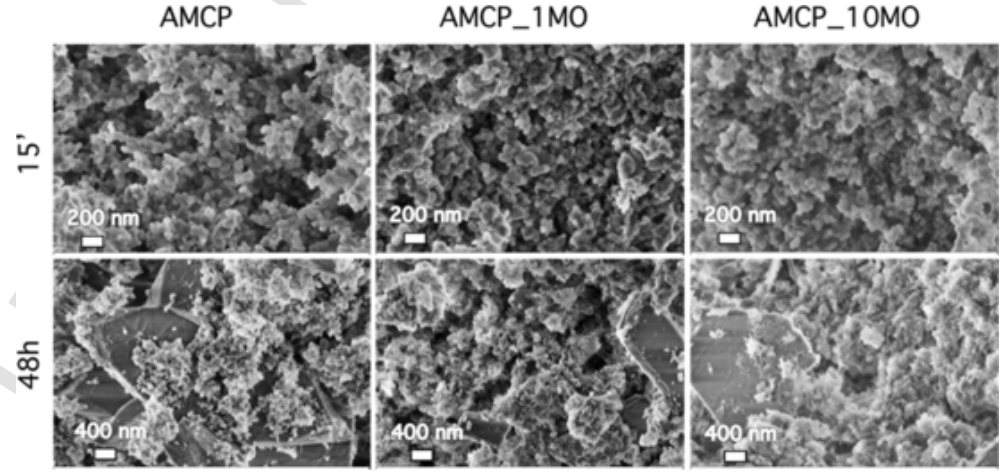

Fig. 3. SEM images of the investigated samples at 15 min and 48 h.

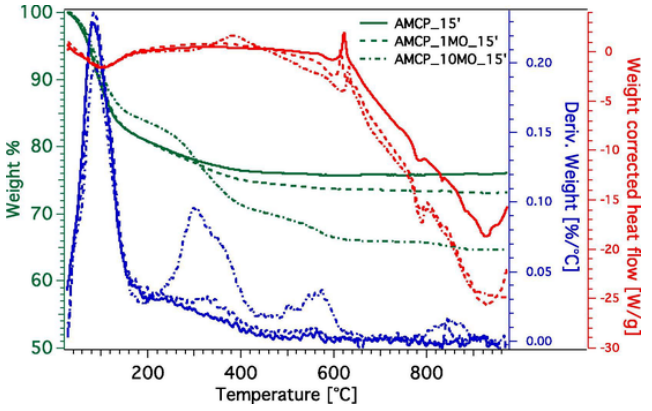

Fig. 4. SDT analysis of samples collected after 15 reaction minutes. Solid line: AMCP_15 min; dashed line: AMCP_1MO_15 min; line and dots: AMCP_10MO_15 min. The green curves refer to the weight % signal, whereas the derivative curves are in blue. The red signals correspond to the heat flow profiles. (For interpretation of the references to colour in this figure legend, the reader is referred to the web version of this article.)

cur at the temperature of pristine AMCP, revealing structural differences in the amorphous phase due to the presence of MO which causes a different degree of ordering in the structure [68,69]. The kinetics of this crystallization event can be further analyzed by calculating the activation energies (E_a) of the processes by means of the Kissinger method [53], which already demonstrated its validity in the characterization of ACP-based systems [68,70–74]. Samples collected after 15 min reaction (AMCP, AMCP_1MO and AMCP_10MO) were therefore analyzed by means of SDT at four heating rates (5, 10, 20 and 50 °C/min), and the obtained heat flow curves are shown in Fig. 5 (A, B, C) and as expected, it was observed that the maximum of the exothermic peak (T_p) shifts to higher T according to the heating rate of the experiment (see Table S1).

The obtained T_p values were used to estimate E_a from the slopes of the Kissinger plots (see Eq. (1)), which are reported in Fig. 5 D, E and F. Table 3 reports activation energies in the order of hundreds of kJ/mol, consistent with those reported for ACP in a recent study [70]. AMCPs prepared with 10 mg/mL of MO display the same E_a as the blank sample, whereas AMCP_1MO is characterized by a higher E_a and interestingly, this is the sample which begins to crystallize at lower T (at β = 10 °C/min, T_p = 615 °C vs 622 °C for AMCP and 633 °C for AMCP_10MO, see Table S1). This last evidence shows that the crystallization process, despite starting at a lower temperature, requires a higher amount of energy, suggesting that the presence of MO during the synthesis leads to a different arrangement of the atoms constituting the amorphous phase, which have to re-organize in order to form the new crystalline phase. Moreover, given the excellent correlation obtained in all cases from the linear fitting of the data (see r^2 in Table 3), it can be concluded that the crystallization is a first order reaction, as this assumption has to be true for the Kissinger model to be valid [70]. For a more precise determination of the reaction order, the heat-induced crystallization process was also analyzed by means of the Borchardt–Daniels method [54]. The crystallization peak with the most symmetric shape, obtained at the heating rate of 10 °C/min, was selected, and the calculation was conducted as described in section 2.2.4. The results, reported in Fig. S4, reveal that the best correlation coefficients are obtained for n = 2/3 in all samples (r^2 = 0.999). Thus, the crystallization process is characterized by a reaction order of 2/3, confirming that the reaction can be approximated as a near first-order reaction as reported in the literature [70].

In order to understand the influence of MO on the nanostructure of the formed particles, amorphous samples (in the form of dry powders) were also characterized by means of SAXS. The experimental curves (Fig. 6) display a typical profile of nanometric structures whose larger size exceeds the range accessible by the instrumental set-up. Data were fitted according to different models, as mentioned in the Materials and Methods and described in detail in the Supporting Information sections. Considering that the samples are investigated in the form of dry powders (to avoid the crystallization of AMCP particles occurring in water), the high concentration of particles in the samples suggests the use of models where inter-particle structure factor is taken into account, such as the Beaucage approach (also known as the Unified Fit model) [56–58] and the fractal model by Teixeira [59]. The inter-particle structure factor (namely, the Percus-Yevick hard spheres structure

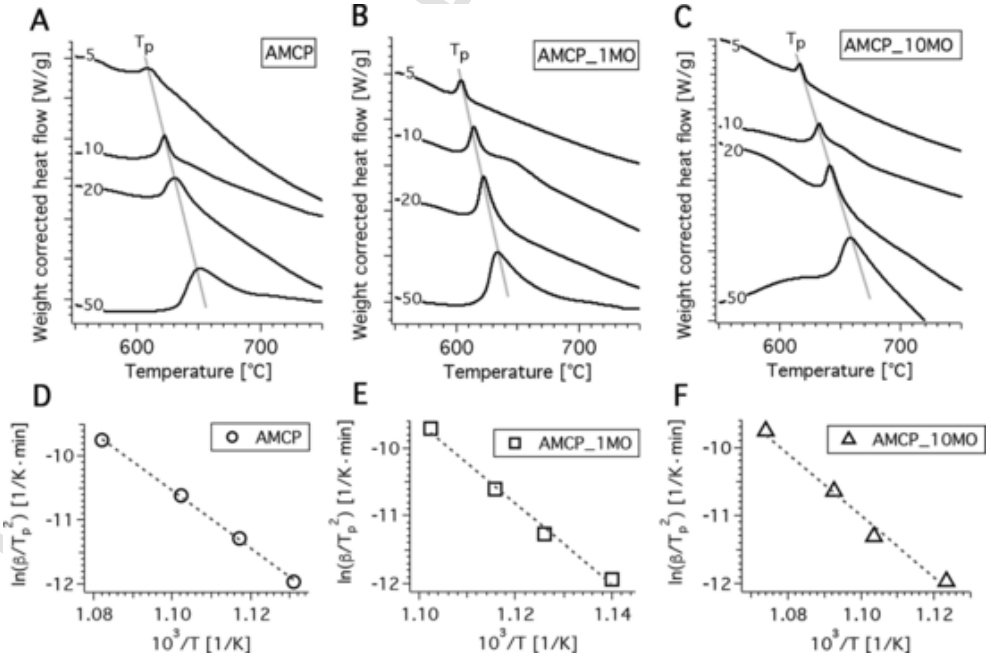

Fig. 5. Kinetic analysis of AMCP heat-induced crystallization by means of the Kissinger method. (A, B, C): heat flow profiles of AMCP_15min (A), AMCP_1MO_15min (B) and AMCP_10MO_15min (C) at 5, 10, 20 and 50 °C/min (heating rate reported on the left of each curve, which are offset for display purposes); (D, E, F): Kissinger plot of AMCP_15min (D), AMCP_1MO_15min (E) and AMCP_10MO_15min (F), according to Eq. (1). The slopes of the lines were used to calculate the activation energies.

Table 3
Data obtained from the kinetic analysis of AMCP heat-induced crystallization by means of the Kissinger method: activation energy and correlation coefficient for the linear fit of data in Fig. 5. The standard deviations associated with the activation energy reflect the uncertainties of T values (±2 K).

Sample	Activation Energy	r^2
AMCP	375 ± 23 kJ/mol	0.999
AMCP_1MO	497 ± 65 kJ/mol	0.993
AMCP_10MO	378 ± 23 kJ/mol	0.987

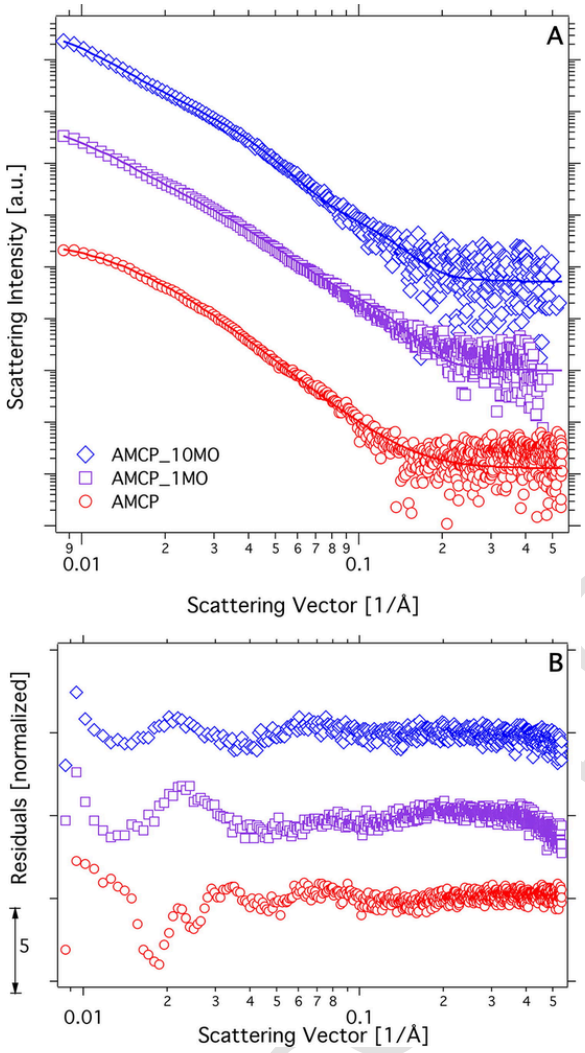

Fig. 6. A: experimental SAXS curves and corresponding fittings for AMCP, AMCP_1MO, and AMCP_10MO according to the Unified Fit model. B: pattern of normalized residuals for each fit. Data are vertically offset for clarity of presentation in both figures.

factor [61]) was included also in the polydisperse core–shell spherical particles [60,75], but the results were not satisfactory (see Supporting Information). This is consistent with the absence of interaction peaks in the low-Q region in the SAXS curves, as it would be expected in the case of rather monodisperse nanoparticles arranged into well-ordered aggregates. In particular, the Beaucage approach has already been shown to provide accurate analysis of inorganic powders [76]. In this model, a general equation describes the scattering from nano- and micro-structured materials in terms of distinct levels. Each level corresponds to a Guinier regime, combined with a structurally limited power-law regime.

For a single structural level, the unified equation is given by:

$$I(Q) \simeq Gexp\left(\frac{-q^2R_g^2}{3}\right) + BQ_{\text{lim}}^{-p} \tag{6}$$

where Q_{lim} structurally limits the power-law at low-q, near R_g, and is given by:

$$Q_{\text{lim}} = \frac{q}{\left[erf\left(qR_g/\sqrt{6}\right)\right]^3} \tag{7}$$

The first term in Eq. (6) describes an exponential scattering decay at a characteristic size, R_g, for one structural level in a material, while the second term describes a power-law decay, which follows the exponential regime. Such scattering has a limit at low q described by the error function *erf*. G is called the Guinier prefactor, R_g is the radius of gyration, and B is the power-law prefactor, described by the regime in which the power-law slope -P falls. For a two-dimensional (2-D), smooth, sharp surface, the power-law follows Porod's law and the slope of a log I versus log q plot is −4.

When more than one structural level is present in a sample, the unified scattering intensity described in Eq. (6) can be extended as:

$$I(Q) \simeq \sum_{i=1}^{n}\left(G_i \exp\left(-q^2R_{g_i}^2/3\right) + B_i exp\left(-q^2R_{g_{(i+1)}}^2/3\right) \times \left\{\left[\text{erf}(qkR_{g_i}/\sqrt{6}\right]^3/q\right\}^{P_i}\right) \tag{8}$$

where n is the number of structural levels. In this last equation, $i = 1$ refers to the largest-size structural level, which consists of fractal aggregates made of smaller sub-units as described by $i > 1$ levels.

Two levels were needed to satisfactorily fit the data for the sample where no MO is present, while three levels were needed in samples including MO (see Fig. 6). The corresponding parameters resulting from the fitting are given in Table 4.

The results of the fitting (see Table 4) show that the presence of the Moringa protein affects the precipitation of AMCP particles, promoting the formation of smaller particles. Due to their strong interaction with calcium, at as low a concentration as 1 mg/mL, MO molecules are able to adsorb onto the surface of newly formed AMCP nuclei, hindering their growth, eventually leading to significantly smaller particle size. Increasing the concentration of MO to 10 mg/mL does not produce a dramatic effect, resulting in the formation of particles whose sizes are similar to the case of 1 mg/mL. These results are consistent with two (possibly coexisting) effects. On one hand, a rough calculation based on the size of the protein and on the amount and size of AMCP particles shows that the concentration of the protein is possibly insufficient to cover the total AMCP surface. This would result in the formation of protein-coated small particles, progressively taking to the consumption of the protein and eventually to an increase of the particle size, finally reaching the same values obtained when Moringa molecules are not present at all. On the other hand, kinetics experiment and previous reports in literature [77] suggest that MO self-assembles into aggregates when the concentration is increased, reducing its ability to cover large surfaces. Unfortunately, SAXS does not allow for an accurate evaluation of the amount of protein adsorbed on the AMCP particles surface. In fact, since the scattering intensity from the MO is very low, as compared to the much higher scattering length density of AMCP, the resulting fitting is poor with inaccuracy of the parameters derived from the fits. It is also worth noting that the SAXS technique probes length-scales much smaller than those accessible by FE-SEM. SAXS provides information about the primary particles that form the larger particles imaged by SEM, such as those in Fig. 3.

Table 4
Parameters values resulting from fitting of the SAXS results for AMCP, AMCP_1MO, and AMCP_10MO according to the Unified Fit model.

Unified Fit Model			
Parameter	AMCP	AMCP_1MO	AMCP_10MO
R_{g1}	63.1 ± 3.9 Å	19.7 ± 0.3 Å	19.4 ± 0.6 Å
P_1	3.48 ± 0.51	3.99 ± 0.07	3.99 ± 0.11
B_1	0.276 ± 0.032	7.24 ± 0.35	4.83 ± 0.21
G_1	23.156 ± 1.502	6.35 ± 0.50	1.79 ± 0.19
R_{g2}	143.4 ± 0.9 Å	60.1 ± 2.0 Å	61.8 ± 1.9 Å
P_2	3.98 ± 0.07	3.51 ± 0.16	3.98 ± 0.28
B_2	$8.21 \cdot 10^{-5} \pm 1.5 \cdot 10^{-6}$	$1.94 \cdot 10^{-5} \pm 5.5 \cdot 10^{-6}$	1.04 ± 0.13
G_2	3130.7 ± 27.3	157.3 ± 5.58	152.1 ± 1.64
R_{g3}	–	210.2 ± 5.3 Å	214.5 ± 9.7 Å
P_3	–	3.89 ± 0.14	3.99 ± 0.18
B_3	–	$7.70 \cdot 10^{-5} \pm 4.3 \cdot 10^{-6}$	$2.79 \cdot 10^{-5} \pm 1.4 \cdot 10^{-6}$
G_3	–	9293.8 ± 223.5	7503 ± 80.7

To understand how the protein is distributed within the amorphous phase, also at the microscale, AMCPs prepared in the presence of MO were analyzed by means of confocal Raman microscopy. AMCP and MO display two distinct signals (see Fig. S10), which were used to carry out a mapping of the AMPC/MO aggregate. AMCP's most intense peak is located at 700–1100 cm^{-1} and corresponds to $\nu_1(PO_4)$ vibrations [78] whereas MO signal at 2800–3100 cm^{-1} is mainly related to C—H stretching. Representative areas were selected on the basis of white light images, shown in Fig. S11, and the obtained maps reported in Fig. 7 show that in both cases MO is located within AMCPs, as no separation between the two signals (*i.e.* red or yellow regions) is visible. These results suggest that, on a micrometer scale, no segregation between AMCP and MO occurs, further supporting the hypothesis that the protein interact with AMCP and is incorporated or absorbed within AMCP structure.

4. Conclusions

The widespread presence of endogenous amorphous calcium and magnesium phosphates, AMCPs, in the human body makes the study of these materials a relevant topic. The development of effective stabilization strategies of the amorphous phases that would allow the use of these materials in nutraceutics and pharmaceutical applications, is an open challenge. This work reports for the first time, to the best of our knowledge, on the effect of proteins from *Moringa oleifera* seeds on the features and crystallization of endogenous-like AMCP particles. From FT-IR and XRD analyses, it was found that these proteins are very effective in delaying the transition from amorphous to crystalline phosphate, as AMCPs synthesized in the presence of 10 mg/mL of MO are over 10 times more stable. This stabilizing effect is MO concentration-dependent and might be connected to a decrease in AMCP solubility, in the presence of the protein. Interestingly, MO not only enhances the lifetime of the amorphous phase, but also influences the type and amount of crystalline material formed. A quantitative Rietveld analysis revealed that, after 48 h of reaction, the amount of amorphous material is larger in the presence of MO, and the protein favors the formation of $Mg_3(PO_4)_2$ over $MgHPO_4{\cdot}3H_2O$. The observed effect is ascribable to the cationic nature of MO, which likely promotes the formation of phosphate over hydrogen-phosphate anions.

Besides the MO effect on the crystallization of AMCPs, the role on the amorphous features at different length scales was examined as well. SAXS analysis shed light on the effect of MO; the presence of the protein results in a strong decrease of the size of the on the formation of AMCP primary particles, which are assembled into sub-micrometric aggregates, as shown by SEM. At the micrometer scale, no MO domains are visible by means of Confocal Raman microscopy, suggesting that the protein is well incorporated within AMCP structure. Applying the Kissinger method to the heat-induced crystallization peak in the AMCP calorimetry data, it was found that the activation energy is significantly higher for the AMCP_1MO sample, suggesting the tendency of MO to self-assemble into aggregates above a certain concentration [77].

In summary, the effect of MO on the features of the amorphous phase and its crystallization pathway were established. The results obtained are relevant both from a fundamental and applied perspective, as demonstrated by the ability of AMCP to load different amount of MO, opening the use of AMPC/MO hybrids in the field of nutraceutics and drug delivery.

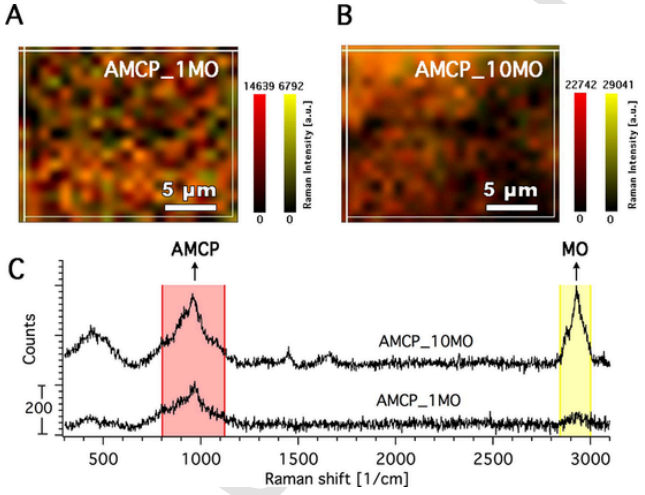

Fig. 7. Confocal Raman maps of (A) AMCP_1MO_15min (A) and (B) AMCP_10MO_15min (B); Raman spectra of AMCP_1MO_15min (bottom) and AMCP_10MO_15min (top) (C), where the red and yellow regions highlight the peaks selected for the mapping. (For interpretation of the references to colour in this figure legend, the reader is referred to the web version of this article.)

Declaration of Competing Interest

The authors declare that they have no known competing financial interests or personal relationships that could have appeared to influence the work reported in this paper.

Acknowledgments

CSGI consortium (Consorzio Interuniversitario per lo Sviluppo dei Sistemi a Grande Interfase), Fondazione CR Firenze (project

2017.0720) and MIUR-Italy ("Progetto Dipartimenti di Eccellenza 2018–2022" allocated to Department of Chemistry "Ugo Schiff") are acknowledged for financial support. Work in Sweden and Namibia was partially supported by the Swedish Research Council (VR/SIDA) Research Links grant with reference 348-2011-7241.

Dr. Laura Chelazzi and Dr. Samuele Ciattini (CRIST, University of Florence) are gratefully acknowledged for their technical support with the diffraction experiments and Rietveld analyses.

This work benefited from the use of the SasView application, originally developed under NSF Award DMR-0520547. SasView also contains code developed funding from the EU Horizon 2020 programme under the SINE2020 project Grant No 654000.

Appendix A. Supplementary material

Supplementary data to this article can be found online at https://doi.org/10.1016/j.jcis.2021.01.008.

References

[1] R. Gelli, F. Ridi, P. Baglioni, The importance of being amorphous: calcium and magnesium phosphates in the human body, Adv. Colloid Interface Sci. 269 (2019) 219–235, doi:10.1016/j.cis.2019.04.011.

[2] J.J. Powell, E. Thomas-McKay, V. Thoree, J. Robertson, R.E. Hewitt, J.N. Skepper, A. Brown, J.C. Hernandez-Garrido, P.A. Midgley, I. Gomez-Morilla, G.W. Grime, K.J. Kirkby, N.A. Mabbott, D.S. Donaldson, I.R. Williams, D. Rios, S.E. Girardin, C.T. Haas, S.F.A. Bruggraber, J.D. Laman, Y. Tanriver, G. Lombardi, R. Lechler, R.P.H. Thompson, L.C. Pele, An endogenous nanomineral chaperones luminal antigen and peptidoglycan to intestinal immune cells, Nat Nano. 10 (2015) 361–369, doi:10.1038/nnano.2015.19.

[3] J. Robertson, C.T. Haas, L.C. Pele, T.P. Monie, C. Charalambos, M. Parkes, R.E. Hewitt, J.J. Powell, Intestinal APCs of the endogenous nanomineral pathway fail to express PD-L1 in Crohn's disease, Sci. Rep. 6 (2016), doi:10.1038/srep26747.

[4] R.E. Hewitt, J. Robertson, C.T. Haas, L.C. Pele, J.J. Powell, Reduction of T-helper cell responses to recall antigen mediated by codelivery with peptidoglycan via the intestinal nanomineral-antigen pathway, Front. Immunol. 8 (2017), doi:10.3389/fimmu.2017.00284.

[5] L.C. Pele, C.T. Haas, R.E. Hewitt, J. Robertson, J. Skepper, A. Brown, J.C. Hernandez-Garrido, P.A. Midgley, N. Faria, H. Chappell, J.J. Powell, Synthetic mimetics of the endogenous gastrointestinal nanomineral: silent constructs that trap macromolecules for intracellular delivery, Nanomed.: Nanotechnol. Biol. Med. 13 (2017) 619–630, doi:10.1016/j.nano.2016.07.008.

[6] S.V. Dorozhkin, Amorphous calcium orthophosphates: nature, chemistry and biomedical applications, Int. J. Mater. Chem. 2 (2012) 19–46, doi:10.5923/j.ijmc.20120201.04.

[7] A.L. Boskey, A.S. Posner, Magnesium stabilization of amorphous calcium phosphate: a kinetic study, Mater. Res. Bull. 9 (1974) 907–916, doi:10.1016/0025-5408(74)90169-X.

[8] B.N. Bachra, H.R.A. Fischer, The effect of some inhibitors on the nucleation and crystal growth of apatite, Calc. Tis Res. 3 (1969) 348–357, doi:10.1007/BF02058677.

[9] F. Abbona, A. Baronnet, A XRD and TEM study on the transformation of amorphous calcium phosphate in the presence of magnesium, J. Cryst. Growth 165 (1996) 98–105, doi:10.1016/0022-0248(96)00156-X.

[10] O. Bertran, L.J. del Valle, G. Revilla-López, M. Rivas, G. Chaves, M.T. Casas, J. Casanovas, P. Turon, J. Puiggalí, C. Alemán, Synergistic approach to elucidate the incorporation of magnesium ions into hydroxyapatite, Chem. – Eur. J. 21 (2015) 2537–2546, doi:10.1002/chem.201405428.

[11] X. Yang, B. Xie, L. Wang, Y. Qin, Z.J. Henneman, G.H. Nancollas, Influence of magnesium ions and amino acids on the nucleation and growth of hydroxyapatite, CrystEngComm 13 (2011) 1153–1158, doi:10.1039/C0CE00470G.

[12] H. Ding, H. Pan, X. Xu, R. Tang, Toward a detailed understanding of magnesium ions on hydroxyapatite crystallization inhibition, Cryst. Growth Des. 14 (2014) 763–769, doi:10.1021/cg401619s.

[13] Q. Liu, Z. Chen, H. Pan, B.W. Darvell, J.P. Matinlinna, Effect of magnesium on the solubility of hydroxyapatite, Eur. J. Inorg. Chem. 2016 (2016) 5623–5629, doi:10.1002/ejic.201601056.

[14] I. Buljan Meić, J. Kontrec, D. Domazet Jurašin, B. Njegić Džakula, L. Štajner, D.M. Lyons, M. Dutour Sikirić, D. Kralj, Comparative study of calcium carbonates and calcium phosphates precipitation in model systems mimicking the inorganic environment for biomineralization, Cryst. Growth Des. 17 (2017) 1103–1117, doi:10.1021/acs.cgd.6b01501.

[15] R. Gelli, M. Scudero, L. Gigli, M. Severi, M. Bonini, F. Ridi, P. Baglioni, Effect of pH and Mg^{2+} on Amorphous Magnesium-Calcium Phosphate (AMCP) stability, J. Colloid Interface Sci. 531 (2018) 681–692, doi:10.1016/j.jcis.2018.07.102.

[16] N.C. Blumenthal, V. Cosma, S. Levine, Effect of gallium on the in vitro formation, growth, and solubility of hydroxyapatite, Calcif. Tissue Int. 45 (1989) 81–87, doi:10.1007/BF02561406.

[17] N.C. Blumenthal, V. Cosma, D. Skyler, J. LeGeros, M. Walters, The effect of cadmium on the formation and properties of hydroxyapatite *In vitro* and its relation to cadmium toxicity in the skeletal system, Calcif. Tissue Int. 56 (1995) 316–322, doi:10.1007/BF00318053.

[18] M.J. Root, Inhibition of the amorphous calcium phosphate phase transformation reaction by polyphosphates and metal ions, Calcif. Tissue Int. 47 (1990) 112–116, doi:10.1007/BF02555994.

[19] T.A. Fuierer, M. LoRe, S.A. Puckett, G.H. Nancollas, A Mineralization adsorption and mobility study of hydroxyapatite surfaces in the presence of zinc and magnesium ions, Langmuir 10 (1994) 4721–4725, doi:10.1021/la00024a054.

[20] J.D. Termine, R.A. Peckauskas, A.S. Posner, Calcium phosphate formation in vitro. II. Effects of environment on amorphous-crystalline transformation, Arch. Biochem. Biophys. 140 (1970) 318–325, doi:10.1016/0003-9861(70)90072-X.

[21] H. Fleisch, R.G.G. Russell, S. Bisaz, J.D. Termine, A.S. Posner, Influence of pyrophosphate on the transformation of amorphous to crystalline calcium phosphate, Calcif. Tissue Res. 2 (1968) 49–59, doi:10.1007/BF02279193.

[22] R.Z. LeGeros, D. Mijares, J. Park, X.-F. Chang, I. Khairoun, R. Kijkowska, R. Dias, J.P. LeGeros, Amorphous calcium phosphates (ACP): formation and stability, Key Eng. Mater. 284–286 (2005) 7–10, doi:10.4028/www.scientific.net/KEM.284-286.7.

[23] Y.-Y. Hu, A. Rawal, K. Schmidt-Rohr, Strongly bound citrate stabilizes the apatite nanocrystals in bone, PNAS 107 (2010) 22425–22429, doi:10.1073/pnas.1009219107.

[24] N.C. Blumenthal, F. Betts, A.S. Posner, Nucleotide stabilization of amorphous calcium phosphate, Mater. Res. Bull. 10 (1975) 1055–1060, doi:10.1016/0025-5408(75)90214-7.

[25] M.R. Christoffersen, J. Christoffersen, The inhibitory effects of ATP, ADP, and AMP on the rate of dissolution of calcium hydroxyapatite, Calcif. Tissue Int. 36 (1984) 659–661, doi:10.1007/BF02405386.

[26] A.S. Posner, F. Betts, N.C. Blumenthal, Role of ATP and Mg in the stabilization of biological and synthetic amorphous calcium phosphates, Calcif. Tissue Res. 22 (1976) 208–212, doi:10.1007/BF02064066.

[27] N.C. Blumenthal, F. Betts, A.S. Posner, Stabilization of amorphous calcium phosphate by Mg and ATP, Calcif. Tissue Res. 23 (1977) 245–250, doi:10.1007/BF02012793.

[28] S.M. Qiu, G. Wen, N. Hirakawa, R.D. Soloway, N.K. Hong, R.S. Crowther, Glycochenodeoxycholic acid inhibits calcium phosphate precipitation in vitro by preventing the transformation of amorphous calcium phosphate to calcium hydroxyapatite, J. Clin. Invest. 88 (1991) 1265–1271, doi:10.1172/JCI115430.

[29] N.C. Blumenthal, A.S. Posner, L.D. Silverman, L.C. Rosenberg, Effect of proteoglycans on in vitro hydroxyapatite formation, Calcif. Tissue Int. 27 (1979) 75–82, doi:10.1007/BF02441164.

[30] N.C. Blumenthal, Mechanisms of inhibition of calcification, Clin. Orthop. Relat. Res. (1989) 279–289.

[31] Y. Li, W. Weng, K. Cheng, P. Du, G. Shen, J. Wang, G. Han, Preparation of amorphous calcium phosphate in the presence of poly(ethylene glycol), J. Mater. Sci. Lett. 22 (2003) 1015–1016, doi:10.1023/A:1024741426069.

[32] Y. Li, W. Weng, In vitro synthesis and characterization of amorphous calcium phosphates with various Ca/P atomic ratios, J. Mater. Sci. Mater. Med. 18 (2007) 2303–2308, doi:10.1007/s10856-007-3132-4.

[33] J. Wang, Y. Chen, L. Li, J. Sun, X. Gu, X. Xu, H. Pan, R. Tang, Remineralization of dentin collagen by meta-stabilized amorphous calcium phosphate, CrystEngComm 15 (2013) 6151–6158, doi:10.1039/C3CE40449H.

[34] Z. Amjad, Inhibition of the amorphous calcium phosphate phase transformation reaction by polymeric and non-polymeric inhibitors, Phosphorus Res. Bull. 7 (1997) 45–54, doi:10.3363/prb1992.7.0_45.

[35] Z. Amjad, Influence of polyelectrolytes on the precipitation of amorphous calcium phosphate, Colloids Surf. 48 (1990) 95–106, doi:10.1016/0166-6622(90)80221-O.

[36] B. Cantaert, E. Beniash, F.C. Meldrum, The role of poly(aspartic acid) in the precipitation of calcium phosphate in confinement, J. Mater. Chem. B 1 (2013) 6586–6595, doi:10.1039/C3TB21296C.

[37] V. Uskoković, Disordering the disorder as the route to a higher order: incoherent crystallization of calcium phosphate through amorphous precursors, Cryst. Growth Des. 19 (2019) 4340–4357, doi:10.1021/acs.cgd.9b00061.

[38] J. Jampilek, J. Kos, K. Kralova, Potential of nanomaterial applications in dietary supplements and foods for special medical purposes, Nanomaterials 9 (2019) 296, doi:10.3390/nano9020296.

[39] F. Anwar, S. Latif, M. Ashraf, A.H. Gilani, Moringa oleifera: a food plant with multiple medicinal uses, Phytother. Res. 21 (2007) 17–25, doi:10.1002/ptr.2023.

[40] S.K. Kansal, A. Kumari, Potential of M. oleifera for the treatment of water and wastewater, Chem. Rev. 114 (2014) 4993–5010, doi:10.1021/cr400093w.

[41] H.M. Kwaambwa, A.R. Rennie, Interactions of surfactants with a water treatment protein from Moringa oleifera seeds in solution studied by zeta-potential and light scattering measurements, Biopolymers 97 (2012) 209–218, doi:10.1002/bip.22014.

[42] M. Moulin, E. Mossou, L. Signor, S. Kieffer-Jaquinod, H.M. Kwaambwa, F. Nermark, P. Gutfreund, E.P. Mitchell, M. Haertlein, V.T. Forsyth, A.R. Rennie, Towards a molecular understanding of the water purification properties of Moringa seed proteins, J. Colloid Interface Sci. 554 (2019) 296–304, doi:10.1016/j.jcis.2019.06.071.

[43] H.M. Kwaambwa, R. Maikokera, F.M. Nermark, Surface activity interactions in aqueous solution of anionic surfactants with a water treatment protein from *Moringa oleifera* seeds, Green Sustain. Chem. 05 (2015) 31, doi:10.4236/gsc.2015.51005.

[44] V. Kalaiselvi, R. Mathammal, S. Vijayakumar, B. Vaseeharan, Microwave assisted green synthesis of hydroxyapatite nanorods using Moringa oleifera flower extract and its antimicrobial applications, Int. J. Vet. Sci. Med. 6 (2018) 286–295, doi:10.1016/j.ijvsm.2018.08.003.

[45] M. Sundrarajan, S. Jegatheeswaran, S. Selvam, N. Sanjeevi, M. Balaji, The ionic liquid assisted green synthesis of hydroxyapatite nanoplates by Moringa oleifera flower extract: a biomimetic approach, Mater. Des. 88 (2015) 1183–1190, doi:10.1016/j.matdes.2015.09.051.
[46] V.O. Kollath, S. Mullens, J. Luyten, K. Traina, R. Cloots, Protein–calcium phosphate nanocomposites: benchmarking protein loading via physical and chemical modifications against co-precipitation, RSC Adv. 5 (2015) 55625–55632, doi:10.1039/C5RA08060F.
[47] P.J.T. Reardon, J. Huang, J. Tang, Morphology controlled porous calcium phosphate nanoplates and nanorods with enhanced protein loading and release functionality, Adv. Healthcare Mater. 2 (2013) 682–686, doi:10.1002/adhm.201200276.
[48] C. Ching Lau, P.J.T. Reardon, J. Campbell Knowles, J. Tang, Phase-tunable calcium phosphate biomaterials synthesis and application in protein delivery, ACS Biomater. Sci. Eng. 1 (2015) 947–954, doi:10.1021/acsbiomaterials.5b00179.
[49] R. Rohanizadeh, K. Chung, Hydroxyapatite as a carrier for bone morphogenetic protein, J. Oral Implantol. 37 (2011) 659–672, doi:10.1563/AAID-JOI-D-10-00005.
[50] A. Ndabigengesere, K. Subba Narasiah, Quality of water treated by coagulation using Moringa oleifera seeds, Water Res. 32 (1998) 781–791, doi:10.1016/S0043-1354(97)00295-9.
[51] R. Maikokera, H.M. Kwaambwa, Interfacial properties and fluorescence of a coagulating protein extracted from Moringa oleifera seeds and its interaction with sodium dodecyl sulphate, Colloids Surf., B 55 (2007) 173–178, doi:10.1016/j.colsurfb.2006.11.029.
[52] H.E. Kissinger, Reaction kinetics in differential thermal analysis, Anal. Chem. 29 (1957) 1702–1706, doi:10.1021/ac60131a045.
[53] H. Schulz, From the Kissinger equation to model-free kinetics: reaction kinetics of thermally initiated solid-state reactions, ChemTexts. 4 (2018) 9, doi:10.1007/s40828-018-0062-3.
[54] H.J. Borchardt, F. Daniels, The application of differential thermal analysis to the study of reaction kinetics, J. Am. Chem. Soc. 79 (1957) 41–46, doi:10.1021/ja01558a009.
[55] M. Doucet, J.H. Cho, G. Alina, J. Bakker, W. Bouwman, P. Butler, K. Campbell, M. Gonzales, R. Heenan, A. Jackson, P. Juhas, S. King, P. Kienzle, J. Krzywon, A. Markvardsen, T. Nielsen, L. O'Driscoll, W. Potrzebowski, R. Ferraz Leal, T. Richter, P. Rozycko, T. Snow, A. Washington, SasView version 4.2, Zenodo, 2018, https://doi.org/10.5281/zenodo.1412041.
[56] G. Beaucage, Approximations leading to a unified exponential/power-law approach to small-angle scattering, J. Appl. Crystallogr. 28 (1995) 717–728, doi:10.1107/S0021889895005292.
[57] G. Beaucage, Small-angle scattering from polymeric mass fractals of arbitrary mass-fractal dimension, J. Appl. Crystallogr. 29 (1996) 134–146, doi:10.1107/S0021889895011605.
[58] B. Hammouda, Analysis of the Beaucage model, J. Appl. Crystallogr. 43 (2010) 1474–1478, doi:10.1107/S0021889810033856.
[59] J. Teixeira, Small-angle scattering by fractal systems, J. Appl. Crystallogr. 21 (1988) 781–785, doi:10.1107/S0021889888000263.
[60] A. Guinier, G. Fournet, Small-Angle Scattering of X-Rays, John Wiley and Sons, New York, NY, 1955.
[61] J.K. Percus, G.J. Yevick, Analysis of classical statistical mechanics by means of collective coordinates, Phys. Rev. 110 (1958) 1–13, doi:10.1103/PhysRev.110.1.
[62] C. Drouet, Apatite formation: why it may not work as planned, and how to conclusively identify apatite compounds, Biomed. Res. Int. 2013 (2013) 490946, doi:10.1155/2013/490946.
[63] C. Combes, C. Rey, Amorphous calcium phosphates: Synthesis, properties and uses in biomaterials, Acta Biomater. 6 (2010) 3362–3378, doi:10.1016/j.actbio.2010.02.017.
[64] P. Sikder, S.B. Bhaduri, Microwave assisted synthesis and characterization of single-phase tabular hexagonal newberyite, an important bioceramic, J. Am. Ceram. Soc. 101 (2018) 2537–2544, doi:10.1111/jace.15404.
[65] R.L. Frost, W. Martens, P.A. Williams, J.T. Kloprogge, Raman and infrared spectroscopic study of the vivianite-group phosphates vivianite, baricite and bobierrite, Mineral. Mag. 66 (2002) 1063–1074, doi:10.1180/0026461026660077.
[66] H.M. Kwaambwa, R. Maikokera, Infrared and circular dichroism spectroscopic characterisation of secondary structure components of a water treatment coagulant protein extracted from Moringa oleifera seeds, Colloids Surf., B 64 (2008) 118–125, doi:10.1016/j.colsurfb.2008.01.014.
[67] E.D. Eanes, I.H. Gillessen, A.S. Posner, Intermediate states in the precipitation of hydroxyapatite, Nature 208 (1965) 365–367, doi:10.1038/208365a0.
[68] J. Vecstaudza, M. Gasik, J. Locs, Amorphous calcium phosphate materials: formation, structure and thermal behaviour, J. Eur. Ceram. Soc. 39 (2019) 1642–1649, doi:10.1016/j.jeurceramsoc.2018.11.003.
[69] R. Gelli, P. Tempesti, F. Ridi, P. Baglioni, Formation and properties of amorphous magnesium-calcium phosphate particles in a simulated intestinal fluid, J. Colloid Interface Sci. 546 (2019) 130–138, doi:10.1016/j.jcis.2019.03.060.
[70] V. Uskoković, S. Marković, L. Veselinović, S. Škapin, N. Ignjatović, D.P. Uskoković, Insights into the kinetics of thermally induced crystallization of amorphous calcium phosphate, Phys. Chem. Chem. Phys. 20 (2018) 29221–29235, doi:10.1039/C8CP06460A.
[71] C.F. Feng, K.A. Khor, S.W.K. Kweh, P. Cheang, Thermally induced crystallization of amorphous calcium phosphate in plasma-spheroidised hydroxyapatite powders, Mater. Lett. 46 (2000) 229–233, doi:10.1016/S0167-577X(00)00176-2.
[72] K.A. Gross, V. Gross, C.C. Berndt, Thermal analysis of amorphous phases in hydroxyapatite coatings, J. Am. Ceram. Soc. 81 (1998) 106–112, doi:10.1111/j.1151-2916.1998.tb02301.x.
[73] C.F. Feng, K.A. Khor, E.J. Liu, P. Cheang, Phase transformations in plasma sprayed hydroxyapatite coatings, Scr. Mater. 42 (1999) 103–109, doi:10.1016/S1359-6462(99)00321-8.
[74] Z. Zyman, M. Epple, A. Goncharenko, D. Rokhmistrov, O. Prymak, K. Loza, Thermally induced crystallization and phase evolution in powders derived from amorphous calcium phosphate precipitates with a Ca/P ratio of 1:1, J. Cryst. Growth 450 (2016) 190–196, doi:10.1016/j.jcrysgro.2016.06.014.
[75] S.R. Kline, Reduction and analysis of SANS and USANS data using IGOR Pro, J. Appl. Crystallogr. 39 (2006) 895–900, doi:10.1107/S0021889806035059.
[76] E.A. Chavez Panduro, T. Beuvier, M. Fernández Martínez, L. Hassani, B. Calvignac, F. Boury, A. Gibaud, Small-angle X-ray scattering analysis of porous powders of $CaCO_3$, J. Appl. Crystallogr. 45 (2012) 881–889, doi:10.1107/S0021889812032219.
[77] M.S. Hellsing, H.M. Kwaambwa, F.M. Nermark, B.B.M. Nkoane, A.J. Jackson, M.J. Wasbrough, I. Berts, L. Porcar, A.R. Rennie, Structure of flocs of latex particles formed by addition of protein from Moringa seeds, Colloids Surf., A 460 (2014) 460–467, doi:10.1016/j.colsurfa.2013.11.038.
[78] C. Rey, O. Marsan, C. Combes, C. Drouet, D. Grossin, S. Sarda, Characterization of calcium phosphates using vibrational spectroscopies, in: B. Ben-Nissan (Ed.), Advances in Calcium Phosphate Biomaterials, Springer, Berlin Heidelberg, Berlin, Heidelberg, 2014, pp. 229–266, doi:10.1007/978-3-642-53980-0_8.